Inorganic Chemistry

Article

pubs.acs.org/IC

# Phase Separation of a Hexacyanoferrate-Bridged Coordination Framework under Electrochemical Na-ion Insertion

Satoshi Kajiyama,[†] Yoshifumi Mizuno,[†,§] Masashi Okubo,*[,†,‡] Ryosuke Kurono,[‡] Shin-ichi Nishimura,[‡] and Atsuo Yamada[‡]

[†]National Institute of Advanced Industrial Science and Technology (AIST), 1-1-1 Umezono, Tsukuba, Ibaraki 305-8568, Japan

[‡]Department of Chemical System Engineering, School of Engineering, The University of Tokyo, 7-3-1 Hongo, Bunkyo-ku, Tokyo, 113-8656, Japan

Supporting Information

**ABSTRACT:** Phase separation and transformation induced by electrochemical ion insertion are key processes in achieving efficient energy storage. Exploration of novel insertion electrode materials/reactions is particularly important to unravel the atomic/molecular-level mechanism and improve the electrochemical properties. Here, we report the unconventional phase separation of a cyanide-bridged coordination polymer, $Eu[Fe(CN)_6]\cdot 4H_2O$, under electrochemical Na-ion insertion. Detailed structural analyses performed during the electrochemical reaction revealed that, in contrast to conventional electrochemical phase separation induced by the elastic interaction between nearest neighbors, the phase separation of $Na_xEu[Fe(CN)_6]\cdot 4H_2O$ is due to a long-range interaction, namely, cooperative rotation ordering of hexacyanoferrates. Kolmogorov-Johnson-Mehl-Avrami analysis showed that the activation energy for the phase boundary migration in $Na_xEu[Fe(CN)_6]\cdot 4H_2O$ is lower than that in other conventional electrode materials such as $Li_{1-x}FePO_4$.

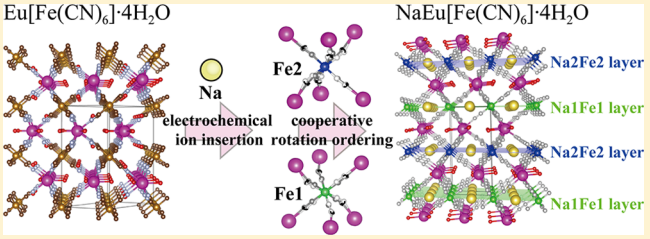


## INTRODUCTION

Phase separation and transformation are subjects of particular importance in the field of materials science, because of their relevance to a number of applications such as sensors, thermoelectrics, and data storage.[1−5] Electrochemical ion insertion, an elemental process of insertion electrode materials for Li- and Na-ion rechargeable batteries, frequently accompanies both phase separation and transformation.[6−12] For example, $LiFePO_4$ olivine, which is a common cathode material in Li-ion batteries, undergoes phase separation into Li-rich and Li-poor phases, and the Li-rich phase is transformed into the Li-poor phase by varying the relative fraction of each phase on charge (Li-ion extraction).[6,13−16] Numerous efforts have been devoted to unraveling the mechanism of electrochemical phase separation and transformation, which is essential for being able to control the rates of both nucleation and boundary migration, as well as for achieving efficient energy storage.[17−20]

On the basis of the elastic interaction between nearest neighbors,[21] the unit cell volume change, $\Delta V$, between the initial and final states is regarded as a primary indicator of whether the system undergoes phase separation during ion insertion: The system shows solid solution Nernst-type behavior for small $\Delta V$ (e.g., 2.0% for $Li_{2-x}FeP_2O_7$)[22] and phase-separating behavior for large $\Delta V$ (e.g., 8.3% for $Na_{3-x}V_2(PO_4)_3$).[8] The large elastic interaction between the nearest neighbors contributes to the positive mixing enthalpy, which leads to phase separation. Despite the importance of $\Delta V$, however, the atomic/molecular-level mechanism of electrochemical phase separation and transformation is not yet fully understood, because of complex coupling of structural changes, boundary migration, ionic/electronic transport, and ionic/electronic correlation.[19,20] In order to tailor electrochemical properties, it is highly desirable to develop electrochemical ion insertion materials that have structural and electronic tunability allowing a microscopic understanding.

Metal organic frameworks (MOFs) have been regarded as promising candidates for exploring novel functionalities, in part due to their structural and electronic tunability.[23−25] In addition, MOFs exhibit structural flexibility, which makes them suitable for constructing robust functionalities upon intercalation of guest species.[5,26] As for electrochemical applications, cyanide-bridged coordination frameworks are among the most widely studied frameworks.[27−31] Orbital hybridization between the metal centers and cyanide ligands provides electronic conductivity, while the porous channel allows guest ions to diffuse in the framework, both of which contribute to enabling electrochemical ion insertion. Many research groups have taken on the challenge to apply them in a wide variety of fields including electrochemical energy storage.[32−41] In the present work, our target is to control phase separation and transformation of cyanide-bridged coordination frameworks under electrochemical ion insertion with tuning structures.

**Received:** December 17, 2013
**Published:** March 3, 2014

   dx.doi.org/10.1021/ic403088r | Inorg. Chem. 2014, 53, 3141−3147

In this work, we report the electrochemical properties of $Eu[Fe(CN)_6]\cdot 4H_2O$. In contrast to conventional phase separation, described by the elastic interaction between nearest neighbors, $Eu[Fe(CN)_6]\cdot 4H_2O$ under Na-ion insertion/extraction exhibits phase separation owing to a long-range cooperative interaction.

## EXPERIMENTAL SECTION

**Synthesis.** $Eu[Fe(CN)_6]\cdot 4H_2O$ was synthesized by a precipitation method. 2.5 mL of an aqueous solution of $Eu(NO_3)_3\cdot 6H_2O$ (0.5 M) was added to an equal volume of an aqueous solution of $K_3Fe(CN)_6$ (0.5 M). The resulting aqueous solution was stirred vigorously for 1 h at 60 °C. Precipitates were filtered and washed with deionized water. After being dried under vacuum, an orange powder was obtained. The chemical composition of $Eu[Fe(CN)_6]\cdot 4H_2O$ was determined by the standard microanalytical method for C, H, and N and by inductively coupled plasma mass spectroscopy for Eu and Fe. Calcd for $Eu[Fe(CN)_6]\cdot 4H_2O$: Eu: 34.86%, Fe: 12.81%, C: 16.53%, N: 19.28%, H: 1.85%. Found: Eu: 34.8%, Fe: 12.7%, C: 16.46%, N: 18.89%, H: 1.76%.

**Analysis.** For electrochemical Na-ion insertion/extraction, three-electrode beaker cells were used. $Eu[Fe(CN)_6]\cdot 4H_2O$ (75 mg, 75 wt %) was ground with acetylene black (20 mg, 20 wt %) and polytetrafluoroethylene (PTFE) (5 mg, 5 wt %) into a paste for the electrochemical experiments. Sodium metal was used for the counter and reference electrodes. As electrolyte, a 1 M $NaClO_4$ propylene carbonate solution was used. The cutoff voltages were 4.0 V for charging (Na-ion extraction) and 2.0 V for discharging (Na-ion insertion). The open circuit voltages (OCV) were recorded by the galvanostatic intermittent titration technique (GITT), where a 10 min slow charge/discharge at 12 mA/g followed by a 30 min interruption process was repeated alternately. The powder X-ray diffraction (XRD) measurements for structural analysis on $Eu[Fe(CN)_6]\cdot 4H_2O$ and $NaEu[Fe(CN)_6]\cdot 4H_2O$ were carried out at BL02B2 of SPring-8, Japan. The wavelength of the X-rays was calibrated to $\lambda$ = 0.6003 Å by a $CeO_2$ standard. Rietveld refinements were conducted using the TOPAS-Academic Ver.5 software. The crystal structure was solved by the structure determination from the powder diffraction (SDPD) procedure, which has been reported elsewhere.[42] *Ex situ* XRD patterns during Na-ion insertion/extraction were recorded with a SmartLab (Rigaku) diffractometer with Cu K$\alpha$ radiation in steps of 0.01° over the range from 10 to 60°. The samples were washed with ethanol after Na-ion insertion/extraction in the GITT mode, then used in the *ex situ* XRD measurements. The unit cell parameters were calculated by least-squares fitting. Thermogravimetric curves (Bruker, 2010SA G4H) for samples were recorded up to 500 °C in air flow condition. For $^{57}Fe$ Mössbauer spectroscopy, $^{57}Co$ in Rh was used as the Mössbauer source. The spectra were calibrated by using six lines of $\alpha$-Fe, the center of which was taken as the zero isomer shift.

## RESULTS AND DISCUSSION

$Eu[Fe(CN)_6]\cdot 4H_2O$ was synthesized by the precipitation method, whereby an aqueous solution of $K_3[Fe(CN)_6]$ and $Eu(NO_3)_3\cdot 6H_2O$ was stirred at 60 °C for 1 h. Both elemental analysis and thermogravimetric measurement (Figure S1, Supporting Information) determine the chemical composition as $Eu[Fe(CN)_6]\cdot 4H_2O$. Though Prussian blue analogs generally contain a large amount of hexacyanoferrate vacancies,[43] the Eu/Fe molar ratio determined by inductively coupled plasma (ICP) spectroscopy is 1.0, which indicates that vacancies are not formed in $Eu[Fe(CN)_6]\cdot 4H_2O$.

On the basis of synchrotron powder X-ray diffraction (XRD) measurement of $Eu[Fe(CN)_6]\cdot 4H_2O$ and the Rietveld refinement (Figure 1a), the crystal structure was successfully refined in the space group *Cmcm*, with unit cell dimensions $a$ = 7.3992(9) Å, $b$ = 12.8285(16) Å, $c$ = 13.6748(17) Å, and $V$ = 1298.0(3) Å$^3$ ($Z$ = 4). The calculated pattern fits the

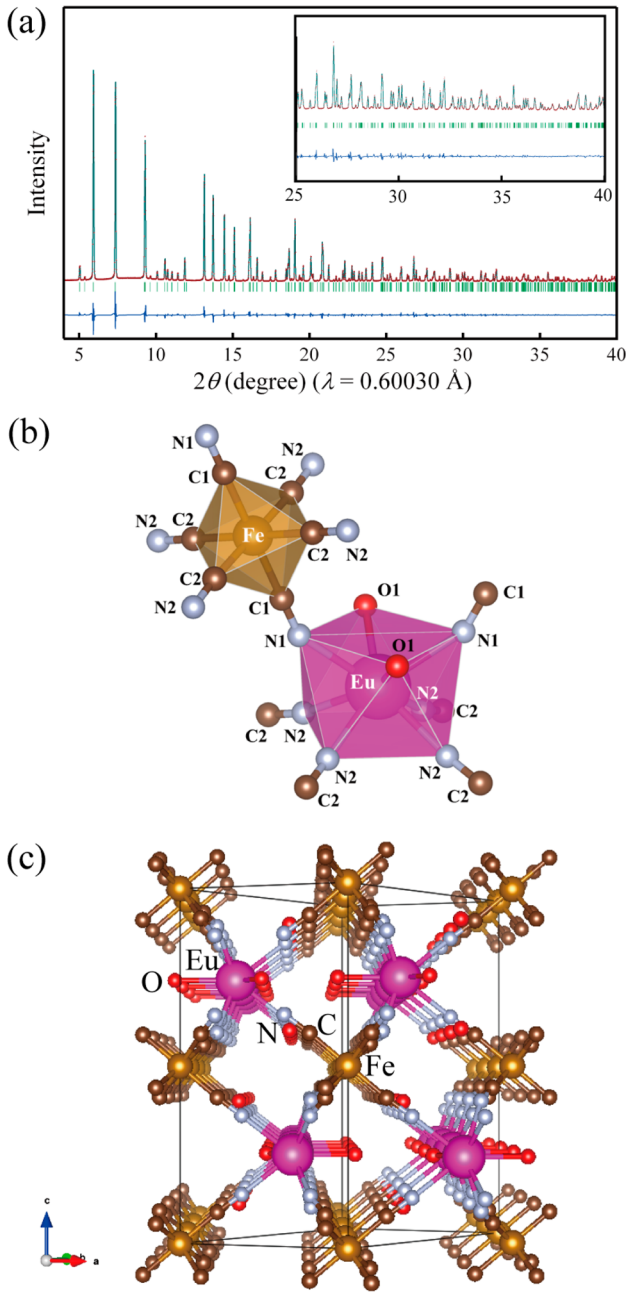


**Figure 1.** (a) Synchrotron powder X-ray diffraction pattern for $Eu[Fe(CN)_6]\cdot 4H_2O$ and the Rietveld refinement ($R_{wp}$ = 6.096%, $R_p$ = 4.419%, $S$ = 2.77, $R_{Bragg}$ = 2.26%); red dots: observed; green line: calculated; blue line: difference. Inset in the figure shows the enlarged patterns from 25 to 40°. (b) Local coordination structure in $Eu[Fe(CN)_6]\cdot 4H_2O$ composed of hexacyanometallate ferricyanide and square antiprism Eu, which are bridged with two crystallographically independent cyanide moieties (C1N1 and C2N2). (c) Crystal structures of $Eu[Fe(CN)_6]\cdot 4H_2O$ along the [1$\bar{1}$0] direction. Solid lines in the image indicate the unit cell.

experimental result well; thus, the obtained compound is a single-phase $Eu[Fe(CN)_6]\cdot 4H_2O$, without any crystalline impurity.

The Rietveld refinement revealed that $Eu[Fe(CN)_6]\cdot 4H_2O$ has one crystsallographically independent Fe metal and two crystallographically independent CN ligands (C1N1 and C2N2). Fe is coordinated equatorially by 4 C of C2N2 and axially by 2 C of C1N1. Eu has a square antiprism geometry


dx.doi.org/10.1021/ic403088r | Inorg. Chem. 2014, 53, 3141−3147

($D_{4d}$), in which one square consists of 4 N of C2N2 while another square consists of 2 N of C1N1 and 2 O of coordinating water (Figure 1b). Both C1N1 and C2N2 bridge between Fe and Eu to form a 3D cyanide-bridged framework with open pore channels along the $[100]_{orth}$, $[110]_{orth}$, and $[1\bar{1}0]_{orth}$ directions (Figure 1c). All these structural characteristics of $Eu[Fe(CN)_6]\cdot 4H_2O$ are the same as isomorphous $Ln[Fe(CN)_6]\cdot 4H_2O$ (Ln = Sm, Tb).[44]

Open circuit voltages (OCVs) for $Eu[Fe(CN)_6]\cdot 4H_2O$ were recorded using the cathodic/anodic galvanostatic intermittent titration technique (GITT)[45] with a Na-ion electrolyte (Figure 2). In Figure 2, the Na-ion content, $x$, in $Na_xEu[Fe(CN)_6]\cdot 4H_2O$ is calculated under the assumption that the electric current during GITT is derived entirely from Na-ion insertion/extraction. The OCVs clearly indicate that the cathodic/anodic reactions occur reversibly with the flat potential plateau at 3.33 V vs $Na/Na^+$. The calculated value of $x$ reaches 1.0 when cathodic GITT finishes. Thermogravimetric measurement after Na insertion shows ca. 12 wt % loss at 120−180 °C, which corresponds to 4 water molecules per the formula unit (Figure S2, Supporting Information). Therefore, the coordinating water remains in the framework even after electrochemical Na-ion insertion, and the end composition is determined as $NaEu[Fe(CN)_6]\cdot 4H_2O$.

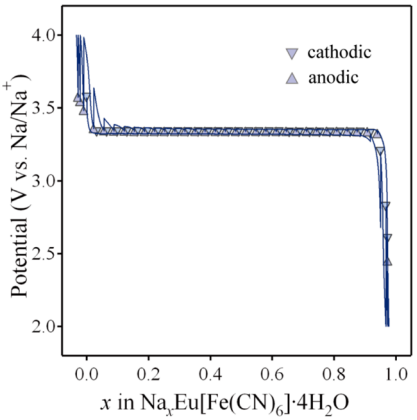


**Figure 2.** Open circuit voltage (OCV) curves for $Eu[Fe(CN)_6]\cdot 4H_2O$. Solid lines are voltage changes during the galvanostatic intermittent titration technique (GITT) measurement; triangles are OCVs recorded after the 30 min interruption intended to bring the system to equilibrium.

The crystal structure of the end composition after cathodic GITT was determined by synchrotron powder XRD measurement. The observed pattern shows clear peak splitting which indicates a distortion of the crystal lattice (Figure 3a). The observed reflections are fully indexed by adopting a triclinic distortion with a prismatic form of the original lattice. The refined lattice parameters are $a$ = 7.254(2) Å, $b$ = 7.322(2) Å, $c$ = 13.663(4) Å, $\alpha$ = 88.6742(9)°, $\beta$ = 91.2030(9)°, $\gamma$ = 117.9398(8)°, and $V$ = 640.9(3) Å$^3$ ($Z$ = 2). The positions of the heavy atoms, i.e., Eu and Fe, are derived by transformation from the original C-centered lattice to the primitive one, while the residual atomic positions are determined by subsequent Rietveld refinements and difference Fourier synthesis. As shown in Figure 3b,c, while the 3D cyanide-bridged framework is maintained, there are two crystallographically independent Na ions (Na1 and Na2) in the unit cell. One Na ion is inserted per formula unit of $Eu[Fe(CN)_6]\cdot 4H_2O$, which is consistent with the electrochemically calculated value of $x$.

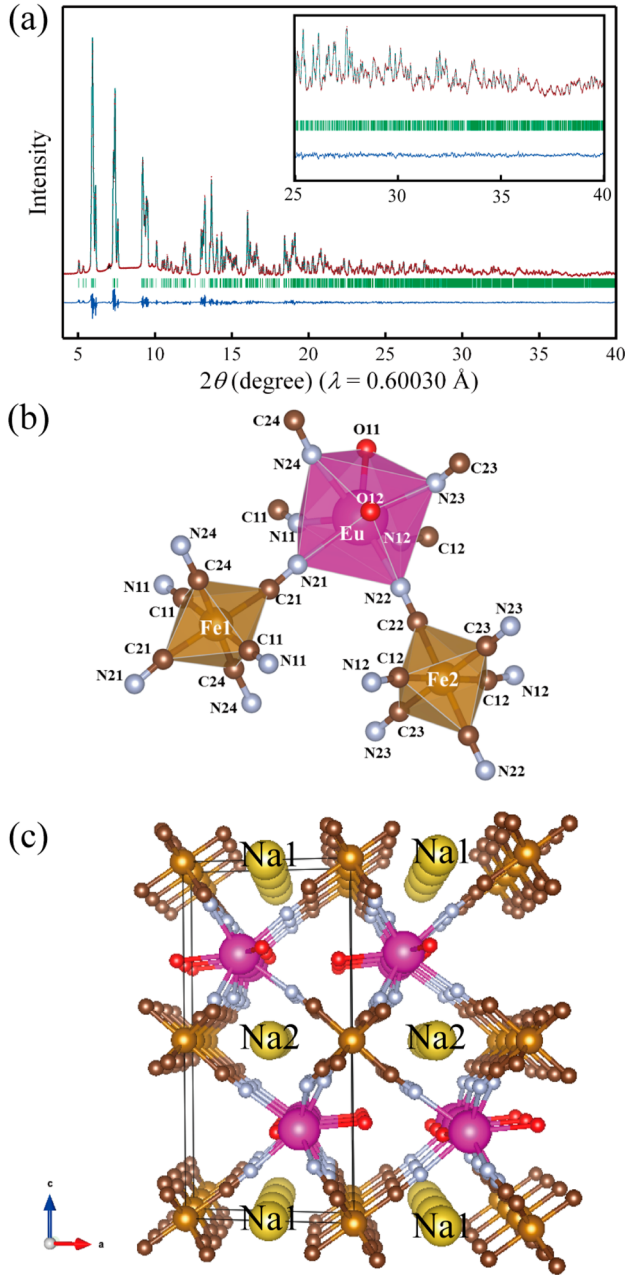


**Figure 3.** (a) Synchrotron powder X-ray diffraction pattern for $NaEu[Fe(CN)_6]\cdot 4H_2O$ and the Rietveld refinement ($R_{wp}$ = 3.669%, $R_p$ = 2.788%, $S$ = 2.04, $R_{Bragg}$ = 1.65%); red dots: observed; green line: calculated; blue line: difference. Inset in the figure shows the enlarged patterns from 25 to 40°. (b) Local coordination structure in $NaEu[Fe(CN)_6]\cdot 4H_2O$. Triclinic $NaEu[Fe(CN)_6]\cdot 4H_2O$ structure is composed of an antiprism square Eu and two crystallographically independent hexacyanoferrate moieties (Fe1 and Fe2). (c) Crystal structure of $NaEu[Fe(CN)_6]\cdot 4H_2O$ along the [010] direction. Solid lines in image indicate the unit cell.

Both Na1 and Na2 occupy the center of the cyanide-bridged $Eu_2Fe_2$ square (Figure 4). The $Eu_2Fe_2$ square shares edges with the adjacent $Eu_2Fe_2$ squares to form open pore channels (Figure 3c). Na1 aligns in the open pore channels along the $[100]_{tri}$ and $[010]_{tri}$ directions (equivalent to the $[100]_{orth}$ and $[1\bar{1}0]_{orth}$ directions in the original orthorhombic cell), in which


dx.doi.org/10.1021/ic403088r | Inorg. Chem. 2014, 53, 3141−3147

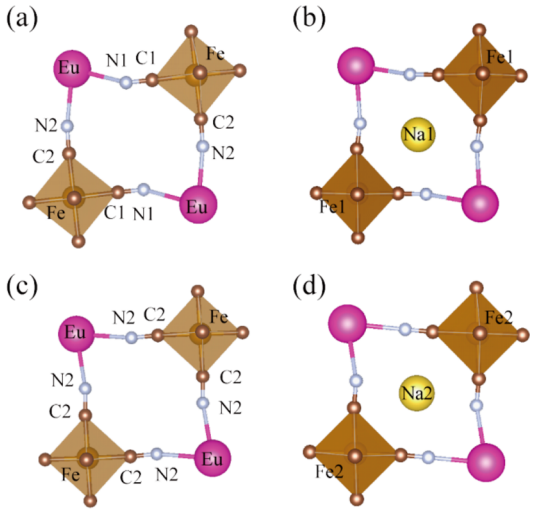


**Figure 4.** $Eu_2Fe_2$ squares surrounding a Na ion. $Eu[Fe(CN)_6]\cdot 4H_2O$ composed of two kinds of $Eu_2Fe_2$ squares: (a) two crystallography independent cyanide moieties (C1N1 and C2N2) bridge between Eu and Fe atoms and (c) one kind of cyanide moieties (C2N2) bridge between Eu and Fe atoms. (b) and (d) show the $Eu_2Fe_2$ structures after Na-ion insertion from image (a) and (c), respectively.

the distance between the Na ions is 7.253(2) and 7.321(1) Å, respectively (Figure S3, Supporting Information). Na2 aligns in the open pore channels along the $[010]_{tri}$ and $[110]_{tri}$ directions (equivalent to the $[1\bar{1}0]_{orth}$ and $[110]_{orth}$ directions), in which the distance between the Na ions is 7.321(1) and 7.513(1) Å, respectively (Figure S4, Supporting Information). On the basis of the Na-ion distribution in $NaEu[Fe(CN)_6]\cdot 4H_2O$, 2D Na-ion diffusion may occur within the *ab* plane.

To confirm the electronic structure change and the amount of inserted Na ions, we carried out $^{57}$Fe Mössbauer spectroscopy (Figure 5 and Table 1). The spectrum of pristine $Eu[Fe(CN)_6]\cdot 4H_2O$ shows a doublet peak, which is typical of an octahedral low-spine $Fe^{III}$ ion in $[Fe^{III}(CN)_6]^{3-}$ (isomer shift (IS) = −0.17 $mms^{-1}$, quadrupole splitting (QS) = 0.76 $mms^{-1}$).[46] After cathodic GITT, the Mössbauer spectrum shows a slightly split peak, which is fitted by two singlet peaks. The IS values are in the range of the previously reported values for an octahedral low-spin $Fe^{II}$ ion in $[Fe^{II}(CN)_6]^{4-}$ (IS = −0.12 and −0.31 $mms^{-1}$).[46] Two singlet peaks are consistent with two crystallographically independent Fe sites in the triclinic cell. Thus, $[Fe^{III}(CN)_6]^{3-}$ in $Eu[Fe(CN)_6]\cdot 4H_2O$ is completely reduced to $[Fe^{II}(CN)_6]^{4-}$ by Na-ion insertion, which confirms that the end composition is $NaEu[Fe(CN)_6]\cdot 4H_2O$. Furthermore, the spectrum of the compound after anodic GITT recovers a doublet peak, as does that of pristine $Eu[Fe(CN)_6]\cdot 4H_2O$. Therefore, electrochemical Na-ion insertion/extraction accompanies the reversible and complete solid-state redox of the $[Fe^{III}(CN)_6]^{3-}/[Fe^{II}(CN)_6]^{4-}$ couple.

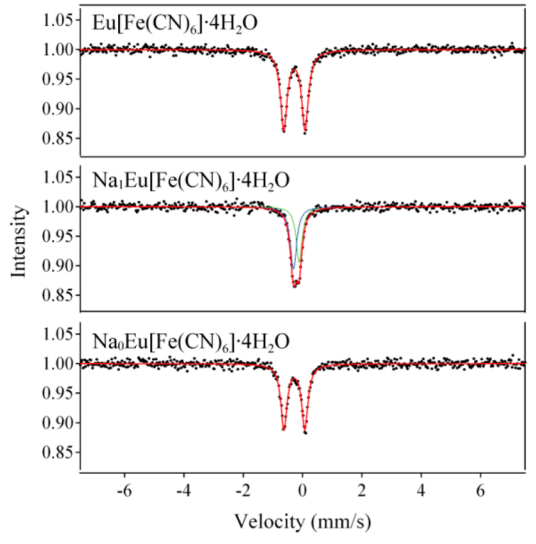


**Figure 5.** Mössbauer (black dots: experimental data; solid lines: fitted curves) for pristine $Eu[Fe(CN)_6]\cdot 4H_2O$, full-discharge $Na_1Eu[Fe(CN)_6]\cdot 4H_2O$, and full-charge $Na_0Eu[Fe(CN)_6]\cdot 4H_2O$.

*Ex situ* XRD patterns obtained during Na-ion insertion/extraction clearly indicate that electrochemical Na-ion insertion/extraction for $Eu[Fe(CN)_6]\cdot 4H_2O$ proceeds through a two-phase process, almost over the entire range of Na-ion concentration (Figures 6a and S5, Supporting Information). When Na-ion insertion starts, new peaks appear in addition to those of the initial orthorhombic phase. The new peaks correspond to triclinic $NaEu[Fe(CN)_6]\cdot 4H_2O$. As Na-ion insertion proceeds, these new peaks increase in intensity at the expense of the original peaks. The original $Eu[Fe(CN)_6]\cdot 4H_2O$ peaks disappear when $x$ reaches 1.0; thus, the entire Na-ion insertion occurs through a two-phase process between $Eu[Fe(CN)_6]\cdot 4H_2O$ and $NaEu[Fe(CN)_6]\cdot 4H_2O$, in perfect agreement with the flat potential plateau in the electrochemical data (Figure 2). The change in the *ex situ* XRD patterns is reversed when Na ion is extracted, indicating the full reversibility of the process. The constant $V/Z$ for each phase indicates that only the relative phase fractions vary on Na-ion insertion/extraction (Figure 6b).

Here, it should be emphasized that the $\Delta V$ between the two phases, 1.4%, is much smaller than that for other two-phase systems such as $Li_{1+x}Mn_2O_4$ (6.0%),[9] $Li_{1-x}FePO_4$ (6.6%),[6] or $Na_{3-x}V_2(PO_4)_3$ (8.3%).[8] The bulk moduli, $K$, of coordination polymers (e.g., 23 GPa for $RbMn[Fe(CN)_6]$ and 11.7 GPa for $Zn(HO_3PC_4H_8PO_3H)\cdot 2H_2O$)[47,48] are generally smaller than those of polyanion compounds (e.g., 90 GPa for $LiFePO_4$).[49] Thus, the elastic interaction between the nearest neighbors in $Eu[Fe(CN)_6]\cdot 4H_2O$ is less pronounced than that in polyanion compounds with the same $\Delta V$. Besides, typical cyanide-bridged frameworks like Prussian blue analogue exhibit a solid solution process even with a $\Delta V$ of 3.5%.[50] Therefore, the nearest neighbor model could not explain the phase separation on the basis of the negligibly small $\Delta V$ for $Na_xEu[Fe(CN)_6]\cdot 4H_2O$.

Another class of two-phase systems is the "zero-strain" system, such as spinel $Li_{4+x}Ti_5O_{12}$ or spinel $Li_{1+x}Rh_2O_4$.[10,51] In the case of $Li_{4+x}Ti_5O_{12}$, for example, even though $\Delta V$ is negligibly small (0.2%) and the true equilibrium state is a solid solution, the apparent two-phase reaction occurs kinetically because of strong Coulombic repulsion between nearest Li ions (interatomic distance: 1.81 Å).[52] However, the distance between Na ions in $NaEu[Fe(CN)_6]\cdot 4H_2O$ is too long (7.25−7.50 Å) to induce a two-phase reaction due to Coulombic repulsion.

We conclude that the phase separation is caused by the long-range cooperative rotation ordering of hexacyanometallates. Comparing the crystal structures of $Eu[Fe(CN)_6]\cdot 4H_2O$ (Figure 1c) and $NaEu[Fe(CN)_6]\cdot 4H_2O$ (Figure 3c) reveals that the structural change occurs mainly through the rotation of the hexacyanoferrates, keeping the Eu−Fe distance almost constant (Figure 7a). Two rotational modes of hexacyanofer-


dx.doi.org/10.1021/ic403088r | Inorg. Chem. 2014, 53, 3141−3147

Table 1. $^{57}$Fe Mössbauer Parameters of $Eu[Fe(CN)_6]\cdot 4H_2O$, $Na_1Eu[Fe(CN)_6]\cdot 4H_2O$, and $Na_0Eu[Fe(CN)_6]\cdot 4H_2O$

| | | isomer shift (mm/s) | quadrupole splitting (mm/s) | fraction (%) |
|---|---|---|---|---|
| $Eu[Fe(CN)_6]\cdot 4H_2O$ | $Fe^{III}$ ($S$ = 1/2) | −0.17 | 0.76 | 100 |
| $Na_1Eu[Fe(CN)_6]\cdot 4H_2O$ | $Fe^{II}$ ($S$ = 0) | −0.12 | 0 | 45.7 |
| | $Fe^{II}$ ($S$ = 0) | −0.31 | 0 | 54.3 |
| $Na_0Eu[Fe(CN)_6]\cdot 4H_2O$ | $Fe^{III}$ ($S$ = 1/2) | −0.17 | 0.75 | 100 |

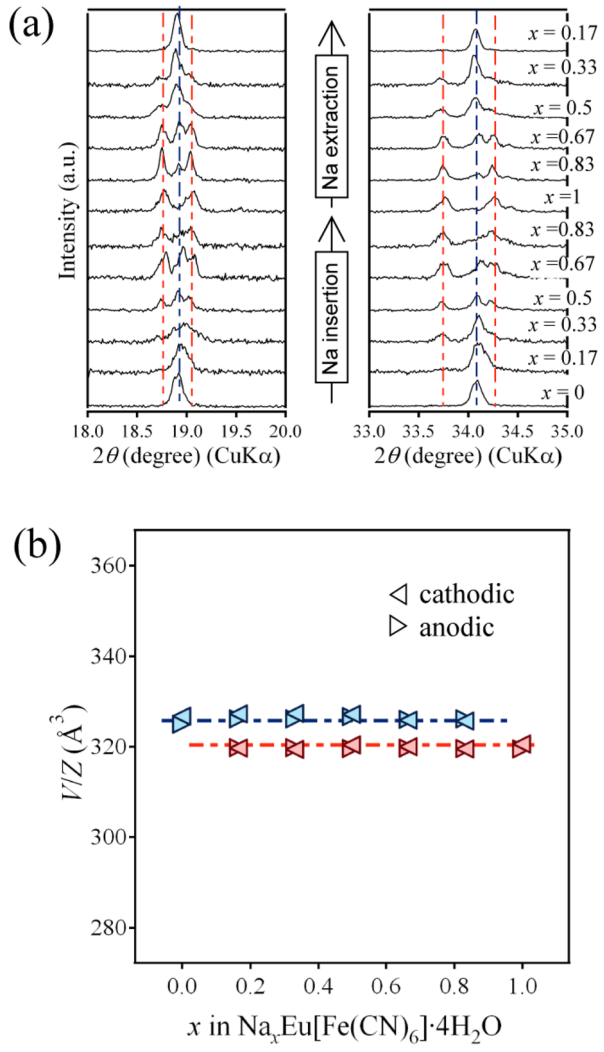


**Figure 6.** (a) *Ex situ* powder XRD patterns during insertion/extraction of Na ions in the GITT mode. Blue dotted lines indicate the peaks of the original orthorhombic phase, while red dotted lines indicate the peaks of the Na-inserted triclinic phase. (b) Unit cell volume per formula unit, $V/Z$, during Na insertion/extraction for $Eu[Fe(CN)_6]\cdot 4H_2O$ (blue triangles) and $NaEu[Fe(CN)_6]\cdot 4H_2O$ (red triangles).

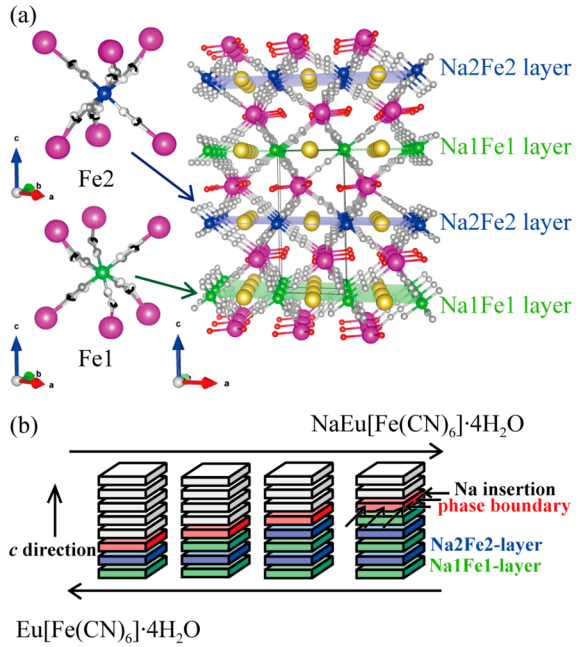


**Figure 7.** (a) Two rotation modes for hexacyanoferrates and alternative stacking of Na1Fe1 and Na2Fe2 layers in the triclinic $NaEu[Fe(CN)_6]\cdot 4H_2O$ structure. (b) Schematic of the domino-cascade mechanism of phase transformation in $Na_xEu[Fe(CN)_6]\cdot 4H_2O$.

rates induced by Na-ion insertion arouse two crystallographically independent Fe sites (Fe1 and Fe2) in $NaEu[Fe(CN)_6]\cdot 4H_2O$, each of which forms a porous cyanide-bridged layer on the *ab* plane (Na1Fe1 layer or Na2Fe2 layer). As Fe positions are fixed during the unit cell change, averaged rotation angle of Fe1−C is ca. 5.9°, while that of Fe2−C is ca. 7.7°. Note that the layers are stacked alternatively along the *c* axis (Figure 7a). The layer consisting of cooperatively rotated hexacyanoferrates causes the hexacyanoferrates in the adjacent layer to exhibit another cooperative rotation, which reduces the interlayer elastic strain. Such long-range interaction, i.e., the cooperative rotation of the hexacyanoferrates in each layer as well as the alternative stacking of the Na1Fe1 and Na2Fe2 layers, presumably stabilizes the triclinic $NaEu[Fe(CN)_6]\cdot 4H_2O$ phase and destabilizes the solid solution state, leading to phase separation.

The cooperative rotation and dominant long-range interaction in $NaEu[Fe(CN)_6]\cdot 4H_2O$ may arise from the weak Eu−N bond, although at this point their mechanism is not completely understood. Certainly, the weak Eu−N bond allows for facile rotation of the hexacyanoferrates to adapt to the Madelung potential perturbed by insertion of Na-ion and electron. Indeed, after Na-ion insertion, three Eu−N bonds become shorter by ca. 0.05 Å while the other bonds become longer by ca. 0.04 Å. Although Eu is a redox inactive site, these changes are comparable with the distance change of the Fe−C bonds in the redox-active hexacyanoferrates, suggesting weak flexible Eu−N bonds. Alternatively, or in parallel, the weak Eu−N bond makes the nearest-neighbor interaction less pronounced, which relatively enhances the importance of long-range interaction.

Taking into account the Na-ion diffusion within the *ab* plane, the domino cascade model,[15] proposed by Delmas et al., predicts 1D boundary migration along the *c* axis (Figure 7b). At the beginning of Na-ion insertion, the $NaEu[Fe(CN)_6]\cdot 4H_2O$ phase nucleates at the particle edge. The Na ions are then inserted into a Fe layer at the phase boundary between $Eu[Fe(CN)_6]\cdot 4H_2O$ and $NaEu[Fe(CN)_6]\cdot 4H_2O$ on the *ab* plane, in which hexacyanoferrates are rotated cooperatively to


dx.doi.org/10.1021/ic403088r | Inorg. Chem. 2014, 53, 3141−3147

form the Na1Fe1 or Na2Fe2 layer depending on the adjacent layer. Then, the phase boundary migrates to vary the fraction of the phases on Na-ion insertion (Figure 7b).

To support the above phase transformation dynamics, we carried out an analysis based on the Kolmogorov-Johnson-Mehl-Avrami (KJMA) model,[53] which assumes a stochastic distribution of nucleation sites, a constant nucleation rate and linear domain growing. In the KJMA model, the volume fraction, $f$, of the equilibrium state is given by $f = 1 - \exp\{-(kt)^n\}$, in which $k$, $t$, and $n$ are the rate constant, time, and Avrami exponent, respectively. $n$ depends on the dimensionality of the phase growth as well as the nucleation homogeneity.

The evolution of $f$ for $NaEu[Fe(CN)_6]\cdot 4H_2O$ was obtained by recording the transient current after application of the potential step from 3.4 to 3.2 V (vs $Na/Na^+$). Figure 8a shows

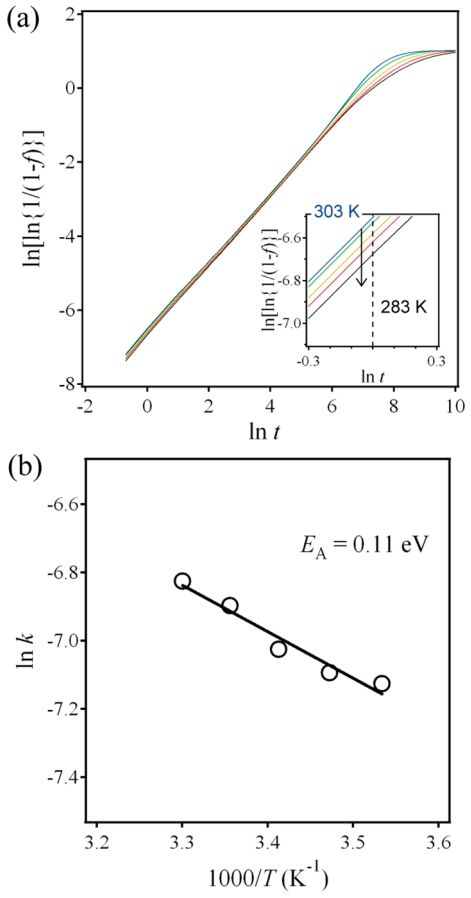


**Figure 8.** (a) Evolution of the phase volume fraction, $f$, of $NaEu[Fe(CN)_6]\cdot 4H_2O$ with time, $t$, under a cathodic potential step of 200 mV (from 3.4 to 3.2 V) at various temperatures (283–303 K). (b) Arrhenius plot of the reaction rate, $k$. Activation energy for phase boundary migration, $E_A$, is calculated with the fitted result (solid line).

the curves of $\ln[\ln(1/(1 - f(t)))]$ vs. $\ln t$ at various temperatures. If the phase transformation follows the KJMA model, the curve should have a slope of $n$ and an intercept of $n\ln k$. All the experimental curves at various temperatures give an $n$ value of almost unity. This suggests that the phase boundaries move in a one-dimensional direction (presumably $c$ direction) during Na-ion insertion. Figure 8b shows an Arrhenius plot of $k$, which gives an activation energy, $E_A$, of 0.11 eV for phase boundary migration. This is much smaller than the $E_A$ for typical two-phase systems like $Li_{1+x}Mn_2O_4$ ($E_A$ = 0.42 eV, $\Delta V$ = 6.0%)[54] and $Li_{1-x}FePO_4$ ($E_A$ = 0.41 eV, $\Delta V$ = 6.6%).[18] The small $E_A$ agrees with the small elastic strain minimized by the cooperative rotation ordering.

## CONCLUSION

We have demonstrated spontaneous phase separation and topotactic transformation of $Eu[Fe(CN)_6]\cdot 4H_2O$ under electrochemical Na-ion insertion/extraction. Although the phase transformation from $Eu[Fe(CN)_6]\cdot 4H_2O$ to $NaEu[Fe(CN)_6]\cdot 4H_2O$ is accompanied by a small volume change, $\Delta V$, of 1.4%, which would not generate sufficient elastic strain to cause phase separation, $Eu[Fe(CN)_6]\cdot 4H_2O$ under Na-ion insertion/extraction clearly shows a two-phase reaction almost over the entire range of Na-ion concentration. We conclude that the phase separation occurs through a long-range interaction, namely, the cooperative rotation ordering of hexacyanoferrates. The present work demonstrates a novel cooperative mechanism whereby an electrochemical phase separation can be induced through the use of coordination framework electrodes.

## ASSOCIATED CONTENT

### Supporting Information

Details of the crystal structure investigations for $Eu[Fe(CN)_6]\cdot 4H_2O$ and $NaEu[Fe(CN)_6]\cdot 4H_2O$, in the form of crystallographic information files (CIFs), thermogravimetric measurements for $Eu[Fe(CN)_6]\cdot 4H_2O$ and $NaEu[Fe(CN)_6]\cdot 4H_2O$, *ex situ* XRD patterns of the samples after Na-ion insertion/extraction in the GITT mode, and SEM image of pristine sample. This material is available free of charge via the Internet at http://pubs.acs.org.

## AUTHOR INFORMATION

### Corresponding Author

*E-mail: m-okubo@aist.go.jp.

### Present Address

[§]Y.M.: Department of Electronic Chemistry, Interdisciplinary Graduate School of Science and Engineering, Tokyo Institute of Technology, Nagatsuta-cho 4259, Midori-ku, Yokohama 226-8502, Japan.

### Notes

The authors declare no competing financial interest.

## ACKNOWLEDGMENTS

Part of this work was financially supported by a KAKENHI on Innovative Areas ("Coordination Programming" Area 2107) from MEXT, Japan. M.O. was supported by the Industrial Technology Research Grant Program in 2010 from the New Energy and Industrial Development Organization (NEDO), Japan. The crystal structure was drawn using the VESTA software.[55]

## REFERENCES

(1) Ito, H.; Muromoto, M.; Kurenuma, S.; Ishizaka, S.; Kitamura, N.; Sato, H.; Seki, T. *Nat. Commun.* **2013**, *4*, 2009.

(2) Ma, J.; Dalire, O.; May, A. F.; Carlton, C. E.; McGuire, M. A.; VanBebber, L. H.; Abernathy, D. L.; Ehlers, G.; Hong, T.; Huq, A.; Tian, W.; Keppens, V. M.; Shao-Horn, Y.; Sales, B. C. *Nat. Nanotech.* **2013**, *8*, 445–451.

(3) Gryn'ova, G.; Marshall, D. L.; Blanksby, S. J; Coote, M. L. *Nat. Chem.* **2013**, *5*, 474–481.

(4) Jordens, S.; Isa, L.; Usov, I.; Mezzenga, R. *Nat. Commun.* **2013**, *4*, 1917.

(5) Sakata, Y.; Furukawa, S.; Kondo, M.; Hirai, K.; Horike, N.; Takashima, Y.; Uehara, H.; Louvain, N.; Meilikov, M.; Tsuruoka, T.; Isoda, S.; Kosaka, W.; Sakata, O.; Kitagawa, S. *Science* **2013**, *339*, 193−196.
(6) Padhi, A. K.; Nanjundaswamy, K. S.; Goodenough, J. B. *J. Electrochem. Soc.* **1997**, *144*, 1188−1194.
(7) Recham, N.; Chotard, J.-N.; Dupont, L.; Delacourt, C.; Walker, W.; Armand, M.; Tarascon, J.-M. *Nat. Mater.* **2010**, *9*, 68−74.
(8) Lim, S. Y.; Kim, H.; Shakoor, R. A.; Jung, Y.; Choi, J. W. *J. Electrochem. Soc.* **2012**, *159*, A1393−A1397.
(9) Thackeray, M. M. *Prog. Solid State Chem.* **1997**, *25*, 1−71.
(10) Colbow, K. M.; Dahn, J. R.; Haering, R. R. *J. Power Sources* **1989**, *26*, 397−402.
(11) (a) Yabuuchi, N.; Kajiyama, M.; Iwatate, J.; Nishikawa, H.; Hitomi, S.; Okuyama, R.; Usui, R.; Yamada, Y.; Komaba, S. *Nat. Mater.* **2012**, *11*, 512−517. (b) Wang, Y.; Yu, X.; Xu, S.; Bai, J.; Xiao, R.; Hu, Y. S.; Li, H.; Yang, X. Q.; Chen, L.; Huang, X. *Nat. Commun.* **2013**, *4*, 2365−2371. (c) Komaba, S.; Yabuuchi, N.; Nakayama, T.; Ogata, A.; Ishikawa, T.; Nakai, I. *Inorg. Chem.* **2012**, *51*, 6211−6220. (d) Wang, X.; Liu, G.; Iwao, T.; Okubo, M.; Yamada, A. *J. Phys. Chem. C* **2014**, *118*, 2970−2976.
(12) (a) Tamaru, M.; Wang, X.; Okubo, M.; Yamada, A. *Electrochem. Commun.* **2013**, *33*, 23−26. (b) Wang, X.; Tamaru, M.; Okubo, M.; Yamada, A. *J. Phys. Chem. C* **2013**, *117*, 15545−15551. (c) Barpanda, P.; Ye, T.; Nishimura, S.; Chung, S. C.; Yamada, Y.; Okubo, M.; Zhou, H. S.; Yamada, A. *Electrochem. Commun.* **2012**, *24*, 116−119. (d) Okubo, M.; Li, C. H.; Talham, D. R. *Chem. Commun.* **2014**, *50*, 1353−1355.
(13) Yamada, A.; Koizumi, H.; Nishimura, S.; Sonoyama, N.; Kanno, R.; Yonemura, M.; Nakamura, T.; Kobayashi, Y. *Nat. Mater.* **2006**, *5*, 357−360.
(14) Sasaki, T.; Ukyo, Y.; Novak, P. *Nat. Mater.* **2013**, *12*, 569−575.
(15) Delmas, C.; Maccario, M.; Croguennec, L.; Cras, F. L.; Weill, F. *Nat. Mater.* **2008**, *7*, 665−671.
(16) Nishimura, S.; Kobayashi, G.; Ohoyama, K.; Kanno, R.; Yashima, M.; Yamada, A. *Nat. Mater.* **2008**, *7*, 707−711.
(17) Malik, R.; Zhou, F.; Ceder, G. *Nat. Mater.* **2011**, *10*, 587−590.
(18) Oyama, G.; Ymada, Y.; Natsui, R.; Nishimura, S.; Yamada, A. *J. Phys. Chem. C* **2012**, *116*, 7306−7311.
(19) Guignard, M.; Didier, C.; Darriet, J.; Bordet, P.; Elkaïm, E.; Delmas, C. *Nat. Mater.* **2013**, *12*, 74−80.
(20) Berthelot, R.; Carlier, D.; Delmas, C. *Nat. Mater.* **2011**, *10*, 74−80.
(21) Christian, J. W. *The theory of transformations in metals and alloys*; Elsevier science Ltd: Oxford, 2002.
(22) Shimizu, D.; Nishimura, S.; Barpanda, P.; Yamada, A. *Chem. Mater.* **2012**, *24*, 2598−2603.
(23) O'Keeffe, M.; Yaghi, O. M. *Chem. Rev.* **2012**, *112*, 675−702.
(24) Ohkoshi, S.; Imoto, K.; Tsunobuchi, Y.; Takano, S.; Tokoro, H. *Nat. Chem.* **2011**, *3*, 564−569.
(25) Lu, G.; Li, S.; Guo, Z.; Farha, O. K.; Hauser, B. G.; Qi, X.; Wang, Y.; Wang, X.; Han, S.; Liu, X.; DuChene, J. S.; Zhang, H.; Zhang, Q.; Chen, X.; Ma, J.; Loo, S. C. J.; Wei, W. D.; Yang, Y.; Hupp, J. T.; Huo, F. *Nat. Chem.* **2012**, *4*, 310−316.
(26) Inokuma, Y.; Yoshioka, S.; Ariyoshi, J.; Arai, T.; Hitora, Y.; Takada, K.; Matsunaga, S.; Rissanen, H.; Fujita, M. *Nature* **2013**, *495*, 461−466.
(27) Itaya, K.; Ataka, T.; Toshima, S. *J. Am. Chem. Soc.* **1982**, *104*, 4767−4772.
(28) Sato, O.; Iyoda, T.; Fujishima, A.; Hashimoto, K. *Science* **1996**, *271*, 49−51.
(29) de Tacconi, N. R.; Rajeshwar, K.; Lezna, R. O. *Chem. Mater.* **2003**, *15*, 3046−3062.
(30) Asakura, D.; Okubo, M.; Mizuno, Y.; Kudo, T.; Zhou, H. S.; Amemiya, K.; de Groot, F. M. F.; Chen, J.-L.; Wang, W.-C.; Glans, P.-A.; Chang, C.; Guo, J.; Honma, I. *Phys. Rev. B* **2011**, *84*, 045117.
(31) Nanba, Y.; Asakura, D.; Okubo, M.; Mizuno, Y.; Kudo, T.; Zhou, H. S.; Amemiya, K.; Guo, J.; Okada, K. *J. Phys. Chem. C* **2012**, *116*, 24896−24901.
(32) Pasta, M.; Wessells, C. D.; Huggins, R. A.; Cui, Y. *Nat. Commun.* **2012**, *3*, 1149.
(33) Wang, L.; Lu, Y.; Liu, J.; Xu, M.; Cheng, J.; Zhang, D.; Goodenough, J. B. *Angew. Chem., Int. Ed.* **2013**, *52*, 1964−1967.
(34) Asakura, D.; Okubo, M.; Mizuno, Y.; Kudo, T.; Zhou, H. S.; Ikedo, K.; Mizokawa, T.; Okazawa, A.; Kojima, N. *J. Phys. Chem. C* **2012**, *116*, 8364−8369.
(35) Mizuno, Y.; Okubo, M.; Asakura, D.; Saito, T.; Hosono, E.; Saito, Y.; Oh-ishi, K.; Kudo, T.; Zhou, H. S. *Electrochim. Acta* **2012**, *63*, 139−145.
(36) Mizuno, Y.; Okubo, M.; Kagesawa, K.; Asakura, D.; Kudo, T.; Zhou, H. S.; Oh-ishi, K.; Okazawa, A.; Kojima, N. *Inorg. Chem.* **2012**, *51*, 10311−10316.
(37) Asakura, D.; Li, C. H.; Mizuno, Y.; Okubo, M.; Zhou, H. S.; Talham, D. R. *J. Am. Chem. Soc.* **2013**, *135*, 2793−2799.
(38) Mizuno, Y.; Okubo, M.; Hosono, E.; Kudo, T.; Zhou, H. S.; Oh-ishi, K. *J. Phys. Chem. C* **2013**, *117*, 10877−10882.
(39) Okubo, M.; Asakura, D.; Mizuno, Y.; Kudo, T.; Zhou, H. S.; Okazawa, A.; Kojima, N.; Ikedo, K.; Mizokawa, T.; Honma, I. *Angew. Chem., Int. Ed.* **2011**, *50*, 6269−6273.
(40) Okubo, M.; Kagesawa, K.; Mizuno, Y.; Asakura, D.; Hosono, E.; Kudo, T.; Zhou, H. S.; Fujii, K.; Uekusa, H.; Nishimura, S.; Yamada, A.; Okazawa, A.; Kojima, N. *Inorg. Chem.* **2013**, *52*, 3772−3779.
(41) Mizuno, Y.; Okubo, M.; Hosono, E.; Kudo, T.; Oh-ishi, K.; Okazawa, A.; Kojima, N.; Kurono, R.; Nishimura, S.; Yamada, A. *J. Mater. Chem. A* **2013**, *1*, 13055−13059.
(42) Nishimura, S.; Natsui, R.; Yamada, A. *Dalton Trans.* **2014**, *43*, 1502−1504.
(43) Ludi, A.; Güdel, H. U.; Rüegg, M. *Inorg. Chem.* **1970**, *9*, 2224−2227.
(44) Zhou, X.; Wong, W. T.; Faucher, M. D.; Tanner, P. A. *J. Solid State Chem.* **2008**, *181*, 3057−3064.
(45) Weppner, W.; Huggins, R. A. *J. Electrochem. Soc.* **1977**, *124*, 1569−1578.
(46) Gütlich, P.; Bill, E.; Trautwein, A. X. *Mössbauer spectroscopy and transition metal chemistry*; Springer-Verlag: Berlin, 2011.
(47) Boukheddaden, K.; Loutete-Dangui, E. D.; Codjovi, E.; Castro, M.; Rodriguéz-Velamazán, J. A.; Ohkoshi, S.; Tokoro, H.; Koubaa, M.; Abid, Y.; Varret, F. *J. Appl. Phys.* **2011**, *109*, 013520.
(48) Gagnon, K. J.; Beavers, C. M.; Clearfield, A. *J. Am. Chem. Soc.* **2013**, *135*, 1252−1255.
(49) Maxisch, T.; Ceder, G. *Phys. Rev. B* **2006**, *73*, 174112.
(50) Okubo, M.; Asakura, D.; Mizuno, Y.; Kim, J.-D.; Mizokawa, T.; Kudo, T.; Honma, I. *J. Phys. Chem. Lett.* **2010**, *1*, 2063−2071.
(51) Gu, Y. P.; Taniguchi, K.; Tajima, R.; Nishimura, S.; Hashizume, D.; Yamada, A.; Takagi, H. *J. Mater. Chem. A* **2013**, *1*, 6550−6552.
(52) Wagemaker, M.; Simon, D. R.; Kelder, E. M.; Schoonman, J.; Ringpfeil, C.; Haake, U.; Lützenkirchen-Hecht, D.; Frahm, R.; Mulder, F. M. *Adv. Mater.* **2006**, *18*, 3169−3173.
(53) Jackson, K. A. *Kinetic Processes*; Wiley-VCH: Weinheim, 2010.
(54) Okubo, M.; Mizuno, Y.; Yamada, H.; Kim, J.-D.; Hosono, E.; Zhou, H. S.; Kudo, T.; Honma, I. *ACS Nano* **2010**, *4*, 741−752.
(55) Momma, K.; Izumi, F. *J. Appl. Crystallogr.* **2011**, *44*, 1272−1276.